1	A simple three-cylinder radiometer and low-speed anemometer to
2	characterize human extreme heat exposure
3	
4	Konrad Rykaczewski, 1,2* Ankit Joshi, 1,2 Shri H. Viswanathan, 1 Sai S. Guddanti, 1 Kambiz
5	Sadeghi, ^{1,2} Mahima Gupta, ¹ Ankush K. Jaiswal, ^{1,2} Krishna Kompally, ¹ Gokul Pathikonda, ¹ Riley
6	Barlett, ^{2,3} Jennifer K. Vanos, ^{2,3} and Ariane Middel ^{2,4,5}
7	
8	1. School for Engineering of Matter, Transport and Energy, Arizona State University, Tempe, AZ,
9	USA
10	2. Julie Ann Wrigley Global Futures Laboratory, Arizona State University, Tempe, AZ, USA
11	3. School of Sustainability, Arizona State University, Tempe, AZ, USA
12	4. School for Arts, Media and Engineering, Arizona State University, Tempe, AZ, USA
13	5. School of Computing and Augmented Intelligence, Arizona State University, Tempe, AZ, USA
14	*corresponding author email: konradr@asu.edu
15	
16 17 18 19 20 21 22 23 24 25 26 27 28 29 30 31 32 33	As populations and temperatures of urban areas swell, more people face extreme heat and are at increasing risk of adverse health outcomes. Radiation accounts for much of human heat exposure but is rarely used as heat metric due to a lack of cost-effective and accurate sensors. To this end, we fuse the concepts of a three-globe radiometer-anemometer with a cylindrical human body shape representation, which is more realistic than a spherical representation. Using cost-effective and readily available materials, we fabricated two combinations of three cylinders with varying surface properties. These simple devices measure the convection coefficient and the shortwave and longwave radiative fluxes. We tested the devices in a wind tunnel and at fourteen outdoor sites during July 2023's record-setting heat wave in Tempe, Arizona. The average difference between pedestrian-level mean radiant temperature (MRT) measured using research-grade 3-way net radiometers and the three-cylinder setup was $0.4\pm3.0^{\circ}$ C (±1 SD). At most, we observed a 10° C MRT difference on a white roof site with extreme MRT values (70° C to 80° C), which will be addressed through discussed design changes to the system. The measured heat transfer coefficient can be used to calculate wind speed below 2 m·s^{-1} ; thus, the three cylinders combined also serve as a low-speed anemometer. The novel setup could be used in affordable biometeorological stations and deployed across urban landscapes to build human-relevant heat sensing networks.
34 35 36 37	Keywords : Absorbed radiation . Mean radiant temperature . Globe thermometer . Cylindrical radiation thermometer . Radiation geometry . Extreme heat

Introduction

Including hyperlocal biometeorological data for human heat exposure assessment in heat action planning and emergency response could help reduce negative health impacts of extreme heat. However, widely available weather forecasts and real-time reports do not provide information on local microclimates, which can vary across small distances (e.g., meters) within a city (Middel and Krayenhoff 2019; Nazarian et al. 2022). Furthermore, air temperature or simple heat indices such as the heat index or humidex do not quantify the totality of heat received by the human body. **Fig.1 A** shows that in addition to air temperature and humidity, the shortwave and longwave radiative heat fluxes experienced by a human along with mean speed and turbulence intensity of the airflow significantly impact heat stress (Ono et al. 2008; Parsons 2014, 2019; Yu et al. 2020; Zou et al. 2020; Xu et al. 2021; Zhou and Niu 2022; Zhou et al. 2022). The turbulence intensity is consistently in the range of 20 to 40% at the pedestrian level, which can even double the convective heat transfer as compared to non-turbulent flow predicted by only using mean air speed (Zou et al. 2020, 2021); but the radiative variables are much more difficult to predict.

Shortwave and longwave radiation fluxes are commonly measured using an array of expensive pyranometers and pyrgeometers (Höppe 1992; Thorsson et al. 2007; Middel and Krayenhoff 2019), respectively. More cost-effective spherical or cylindrical radiometers are available (Brown and Gillespie 1986; De Dear 1988; Thorsson et al. 2007; Kenny et al. 2008; Brown 2019) but only measure total absorbed radiation. These radiometers also require theoretical accounting for convective heat losses that can often introduce 10 to 20°C errors in the mean radiant temperature (MRT) (Vanos et al. 2021). Wind speed is the primary input into the empirical heat transfer coefficient correlations. However, wind speed is often low during extremely hot periods (i.e., mostly below 1 m·s⁻¹) (Vanos et al. 2021); hence, cost-effective radiometers must be used with expensive high-end anemometers, as many standard propeller- or cup-based devices have a 1 m·s⁻¹ starting threshold.

This study aims to demonstrate a simple and easy-to-fabricate three-cylinder shortwave and longwave radiometer that also measures the cylinders' convection coefficient. We fuse the idea of a three-globe radiometer-anemometer previously developed by Nakayoshi (Nakayoshi et al. 2015a, b) with a cylindrical representation of the human body. As compared to spheres, cylinders provide a more accurate representation of the human body in this context (Fiala et al. 1999; Fiala and Havenith 2015; Staiger and Matzarakis 2020; Rykaczewski et al. 2022a; Viswanathan et al.

2023). The plot in **Fig.1 B** and **C** shows that projected radiation area factors, which are a measure of the fraction of body surface area exposed to direct solar radiation (Fanger 1972; Parsons 2014), for cylinders with different aspect ratios match those of diverse "rotationally symmetric" humans for most solar zenith angles (Park and Tuller 2011; Rykaczewski et al. 2022a, b). In contrast, a sphere's projected radiation area factor is constant and does not represent the human body well. Using cylinders also facilitates uniform placement of internal heaters, which can be challenging within a sphere.

Using cost-effective and readily available materials, we fabricated two combinations of three-cylinder with varying surface properties. We extensively tested the devices in a lab-based wind tunnel and at fourteen outdoor sites during the July 2023 record-setting heat wave in Tempe, AZ, paired with a state-of-the-art mobile biometeorological station (MaRTy) (Middel and Krayenhoff 2019). We compare the shortwave, longwave, total radiation, and MRT values calculated using the integral radiation measurement (IRM) and the three-cylinder methods and discuss reasons for any observed discrepancies. Using spherical geometrical weighting factors in the IRM method, we also assess the impact of switching from globe to cylindrical radiometer geometry on the radiative measurements. The convective heat transfer results are compared against prior correlations and used to evaluate the possibility of employing the cylinders as low-speed anemometers for augmenting low-cost but high-start threshold devices. We conclude by discussing the limitations of the current devices and future improvements that can resolve them.

Methods

Theoretical basis

The schematic of the three-cylinder device in **Fig.1 D** shows that cylinders are heated with internal heat generation (Q), incident shortwave (S_i) , and longwave (L_i) radiation while being cooled through convection and longwave surface radiation emission. As in prior work on three-globe anemometer-radiometer (Nakayoshi et al. 2015a), we show in SI Sections I.1-2 that performing energy balance on the three cylinders yields three equations with the heat transfer coefficient (h), S_i , and L_i being the only unknowns. In the SI Section A, we describe the general solution as well as its major simplifications that can be obtained by carefully setting heater input values and selecting surface coatings such that α_L of at least two cylinders are approximately equal and/or having one with $\alpha_L \approx 0$. We demonstrate this simplification with a combination of heated

black (subscript BH), unheated black (subscript B), and unheated white (subscript W) cylinders and a combination of heated polished (subscript PH), unheated white (subscript W), and unheated black (subscript B) cylinders (see **Fig.1 E** and **Fig.1 F**). We refer to the first combination of cylinders as BHBW and the second as PHBW. We note that the BHBW combination of coatings was also used in prior work on the three-globe anemometer-radiometer (Nakayoshi et al. 2015a).

Device fabrication

We fabricated the devices using 0.4 mm thin aluminum tubes (OD of 0.95 cm cut to a 9.5 cm), T-type micro-thermocouple, self-adhering thin-film resistive heaters, and expandable foam (see **Fig.1 E**). The foam inserts presses the heaters into the walls prevent significant airflow within the cylinders, which was linked to temperature non-uniformities and skewed radiation measurements in prior work with radiation thermometers (Wang and Li 2015). We found that placing a 0.5 by 1 cm piece of metalized taped over the thermocouple (epoxied to the outside) shielded it effectively from the airflow and eliminated the dependence of the heat transfer coefficient on the relative airflow to thermocouple orientation (see the SI Section B.4). Images of all the assembly steps and a more detailed description are shown in the SI Section A.6.

We spray-painted the devices to provide black and white exterior finishes. After measuring the spectral absorptivity (see the SI Section A.6), we calculated the hemispherical spectral band absorptivity for the shortwave (i.e., α_S) and longwave (i.e., α_L) regions by integrating with Planck's emissive power distribution of a black-body at 5527°C (5800 K) and 27°C (300 K), respectively (Bergman et al. 2011). The white coating has $\alpha_{SW} = 0.33$ and $\alpha_{LW} = 0.92$, the black coating has $\alpha_{SB} = 0.95$ and $\alpha_{LB} = 0.95$, and the polished aluminum surface has $\alpha_{SPH} = 0.24$ and $\alpha_{LPH} = 0.01$. Consequently, the black and white coatings satisfy the $\alpha_{LW} \approx \alpha_{LB}$ assumption, and the polished surface satisfies the $\alpha_{LPH} \approx 0$ assumption needed to simplify the general solution.

Roof site sunrise-to-sunset measurements

We conducted measurements during two cloudless days (July 19th and 25th of 2023) using MaRTy, the PHBW and BHBW combinations of three-cylinder devices, and a 3D ultrasonic anemometer (CSAT3B from Campbell Scientific) on an unobstructed site on the southeast edge of the roof of the Walton Center for Planetary Health (33.421°N, 111.926°W, about 30 m elevation above the ground level—see **Fig.2A-D**). The roof is covered with a soft white rubber coating that,

based on the ratio of impinging and reflected solar radiation at the highest solar elevation angle (about 76°), has a local albedo of about 0.35. The sky view factor (SVF) at the 1.2 m center height of the cylinders and height of MaRTy radiation sensors was 0.99. To prevent most shading effects, we placed MaRTy about 1.5 m from the cylinder tripod, oriented the cylinder array to face east, and mounted the 3D ultrasonic anemometer on the same tripod about 30 cm below the cylinders. We recorded the three components of the air velocity at a rate of 20 Hz, sufficient to capture wind turbulence characteristics (Tabrizi et al. 2015; Zou et al. 2021). We note that based on wind tunnel measurements, transient heat transfer modeling, and analysis of outdoor mean wind speed changes and resulting cylinder temperature changes (all described in depth in the SI Sections B and C), we arrived at the 60 s cylinder temperature averaging period being appropriate to ensure the thermal equilibration.

All experiments were conducted along with the MaRTy biometeorological station that measures air temperature, humidity, wind speed, and 6-directional shortwave and longwave radiation. These instruments are described in depth in Middel et al. (Middel and Krayenhoff 2019), while the details of the cylinder array mounting and power delivery are described in depth in the SI. Employing standard $\alpha_{S-MRT}=0.70$ and $\alpha_{L-MRT}=0.97$ that represent skin and clothing properties, we calculated MRT from the incident shortwave and longwave radiation using the Stefan-Boltzmann law:

$$MRT = \sqrt[4]{\frac{\alpha_{S-MRT}S_i + \alpha_{L-MRT}L_i}{\sigma\alpha_{L-MRT}}} - 273.15 \tag{1}$$

Multisite pedestrian-level measurements

We also conducted mid-day (12:00 to 14:30 h) measurements on July 26th of 2023 across an additional thirteen pedestrian-level sites in Tempe, Arizona. All conditions during this period were stable, with air temperature varying only between 43 to 45°C at the different sites (the air temperature did not change during the short measurement period at each site), solar elevation angle around 70°. The different sites along with their bottom-up fish-eye images are mapped in **Fig.2E** and described the corresponding surface and sky/shade characteristics in **Table 1** and SI Section C.8. The sites include fully sun-exposed areas over distinct surfaces (varying from asphalt, concrete, and grass), partially-exposed urban canyons and courtyards, and spaces covered by a variety of natural (native and non-native trees) and industrial shade (fabric sun sail, perforated

metal sheet, and movable solar panels). Ensuring a steady state was reached, we sequentially conducted the radiation measurements in the same location for three-minute periods using first MaRTy and then the three-cylinder array. As in our prior work comparing radiation sensors (Vanos et al. 2021), we quantify the mean difference, mean absolute difference, and the root mean square difference between the different approaches.

166

167

168

169

170

171

172

173

174

175

176

177

178

179

180

181

182

183

184

185

186

187

188

189

190

165

161

162

163

164

Results

Sunrise-to-sunset convection measurements on an unobstructed roof site

Our wind tunnel experiments demonstrated that the heated cylinder provides a simple, cost-effective way to accurately measure the heat transfer coefficients (h) in steady and non-turbulent airflow (see detailed description in the SI Section B). Before discussing the heat transfer coefficients measured in chaotic outdoor flow, we discuss the processing of the wind measurements and their characteristics.

Following Zou et al. (2020, 2021) and Zhou and Niu (2022) we used empirical mode decomposition (EMD) to separate the measured wind speed into time-varying mean $(\bar{V}(t))$ and fluctuating (v'(t)) components (see the detailed description of the process in the SI Section C.4-5). In agreement with prior analyses (Zou et al. 2020, 2021; Zhou and Niu 2022), traditional averaging for one-minute segments yields mean speed values that closely match those from EMD analysis but overestimates the turbulence intensity (TI) by 10 to 20% (see the SI Section C.4). The plot in Fig.3 A shows that on July 25th, the $\bar{V}(t)$ was mostly below 1 m·s⁻¹ in the morning and slowly built throughout the day, fluctuating between 1 and 3 m·s⁻¹. The inset histogram in Fig.3 B shows that about 50% and 75% of measured $\bar{V}(t)$ during both days are below 1 m·s⁻¹ and 1.5 m·s⁻¹ ¹, respectively. The equivalent histogram for TI shows that it is normally distributed around about 30% with a standard deviation of 6% (i.e., about 95% of the turbulence intensity values are between 20 and 40%). The main plot in **Fig.3 B** shows that the TI is nearly independent of the $\overline{V}(t)$ and matches closely with prior measurements taken at the pedestrian level in multiple urban sites in Sydney, Australia (Zou et al. 2020). In particular, the TI vs. $\bar{V}(t)$ fit to our data (the dark orange line in Fig.3 B) matches that reported by Zou et al. (2020) (the blue line in Fig.3 B). Also, the 90th percentile of Zou et al. (2020) TI measurements (the gray area in Fig.3 B) matches the spread of our data.

At sunrise on July 25th, the air temperature was 32°C, gradually increased to a maximum of 46.2°C in the early afternoon and remained above 45°C until sunset (see **Fig.3** C). The surface temperatures of the unheated cylinders followed the same trend but with about 3°C and 10°C offset for the white and black cylinders, respectively. The temperatures of the polished and black cylinders that were heated by 1.5 W were similar, and about 15°C to 20°C warmer than air. We calculated the corresponding heat transfer coefficients by substituting these temperatures into **Eq.I.6** for the BHBW combination of cylinders and **Eq.I.12** for the PHBW combination of cylinders (see the SI Section I.2).

The plot in Fig.3 D shows that the heat transfer coefficients calculated using data from the two combinations of cylinders match closely with differences not exceeding 10% (mean difference of -1.2+1.6 W·m⁻²°C⁻¹(+ 1 SD), mean absolute difference of -1.6+1.1 W·m⁻²°C⁻¹, and root mean square difference of 1.9 W·m⁻²°C⁻¹, which are all within the measurement uncertainty). The values of the heat transfer coefficients are in the range of 20 to 50 W·m⁻²°C⁻¹, as expected based on the wind tunnel measurements for the 0.2 and 4 m·s⁻¹ wind speed range (see the SI Section B). Fig.3 E shows that despite the high level of TI, the heat transfer coefficients measured using the threecylinder devices match closely with the Hilpert and Churchill-Bernstein correlations for no turbulence conditions (the two correlations are described in the SI Section B.2). The two correlations agree closely, with the main advantage of the Hilpert one being a much simpler functional form for our wind speed range (which will be helpful in the discussion section). The Hilpert correlation with $\bar{V}(t)$ input provides an excellent prediction of the measured heat transfer values (see Fig.3 F) with a mean difference of only -0.26±3.2 W·m⁻²°C⁻¹ (± 1 SD), mean absolute difference of -2.4±1.9 W·m⁻²°C⁻¹, and root mean square difference of 3.1 W·m⁻²°C⁻¹. In other words, our measurements demonstrate that the heat transfer coefficient for the cylinders does not depend on the turbulence intensity in the 0.2 and 3.0 m·s⁻¹ wind speed range.

Sunrise-to-sunset radiation measurements on an unobstructed roof site

On July 25th, the solar elevation angle peaked at 76° around 12:30 h, corresponding to maximum horizontal shortwave radiation fluxes of 1090 W·m⁻² and 385 W·m⁻² in the incoming (upward "U" facing sensor) and outgoing (downward "D" facing sensor) directions, respectively (see **Fig.4 A** and **B**). The shortwave fluxes measured using the vertically-oriented pyranometers (east, west, south, and north facing) display more complex trends. In particular, the fluxes are

above the diffuse background when the sensors are exposed to direct solar radiation (e.g., east and north-facing in the morning). The corresponding morning and afternoon fluxes, such as on the west and south-facing sensors, are likely slightly asymmetrical due to the site's geometry (e.g., mild but slight roof slope). The 30-minute drop in radiation on the south-facing pyranometer around 18:00 h is a self-shading artifact (see the SI Section C.2). In contrast to the highly varying shortwave fluxes, the longwave fluxes measured by MaRTy's pyrgeometers display only a minor variation throughout the day (see **Fig.4 C**).

The longwave heat fluxes (L) on the vertically oriented pyrgeometers (east "E", west "W", south "S", and north "N" facing) are nearly equal and only vary between 450 and 600 W·m⁻² throughout the day. The downward ("D") facing pyrgeometer measures the longwave emission from the hot roof surface, which peaks at 730 W·m⁻² around 14:00 h. In the IRM, the directional shortwave (S) and longwave fluxes are combined into a single flux per spectral region that a person would be exposed to using geometrical weights ("W") (Höppe 1992):

$$S_{IRM} = W_{U,D}(S_U + S_D) + W_S(S_E + S_W + S_S + S_N)$$
 (2)

236
$$L_{IRM} = W_{U,D}(L_U + L_D) + W_S(L_E + L_W + L_S + L_N)$$
 (3)

For an average adult standing person (male or female), Hoppe (Höppe 1992) obtained a $W_S=0.22$ geometrical weight for the side-facing sensors by averaging projected area factors measured by Fanger (1972) over all possible directions. This calculation is equivalent to taking an average of the values representing an average male with hands along the body (green curve) in **Fig.1** C across all zenith angles. When calculated this way, the W_S is essentially independent of the human body shape (Rykaczewski et al. 2022a). Accordingly, the geometrical weight for the upwards and downwards-facing sensors is $W_{U,D}=(1-4\cdot22)/2=0.06$. As stated in the introduction and **Fig.1C**, the projected area factors for the human bodies and cylinders are surprisingly similar. In other words, the shortwave and longwave fluxes combined using the IRM approach (i.e., **Eq.2** and 3) and their summation (i.e., total incident radiation equal to $R_t=S_{IRM}+L_{IRM}$) provide an excellent benchmark for the values measured using the three-cylinder devices. To gauge the impact of switching the geometry of the devices from three globes (Nakayoshi et al. 2015a) to three-cylinders, we also calculate the fluxes (and MRT) using the geometrical weight for a sphere (0.167 in all directions).

Both three-cylinder devices yield shortwave heat fluxes that match closely with the IRM values. The shortwave heat flux increases rapidly from sunrise until 9:00 h and remains at 350 to

450 W·m⁻² until 16:00 h. It rapidly decreases after that until sunset. The shortwave heat fluxes obtained using the PHBW and BHBW three-cylinder combinations follow the IRM values closely and deviate at most by 10% (see green line **Fig.4 D**). Owning to increased geometrical weighting of the significant downward and upward components, the IRM shortwave flux calculated using spherical geometrical weights is substantially higher from 9:00 to 15:00 h (up to 90 W·m⁻² or 25%) than the fluxes calculated using the standard values and measured using the three-cylinder devices.

The variation in the IRM longwave flux is much more minor than that of the shortwave flux, with the sunrise value of 450 W·m⁻² increasing to a maximum of 600 W·m⁻² around 14:00 h (see **Fig.4 E**). The longwave heat fluxes obtained using the PHBW and BHBW three-cylinder combinations again match each other closely (see green line in **Fig.4 E**) but underpredict the IRM values by 50 to 100 W·m⁻² from about 7:00 to 15:00 h. In contrast to the large impact on the shortwave flux, employing spherical geometrical weights in the IRM calculation has a minor impact on the longwave flux. This minor difference stems from relatively small variations in the directional longwave fluxes and balancing on the downward and upward fluxes.

The observed differences in the shortwave and longwave fluxes stemming from different approaches propagated into the total incident radiation and MRT time series are shown in Fig.4 F and Fig.5A. Specifically, the underprediction of the longwave heat flux by the three-cylinders compared to the IRM results in an underprediction of the total heat flux by about 100 W·m⁻². A similar magnitude overprediction in the total incident radiation is associated with the overprediction of the shortwave flux stemming from spherical geometrical weight factors (compared to standard geometrical factors representing the human body). In terms of MRT, the three-cylinders underpredict it compared to IRM by 5 to 10°C or about 5 to 15% from about 8:00 to 14:00 h. In direct comparison between the corresponding MRTs from the IRM and threecylinder methods in Fig.5 B, the numerous data points collected during this period heavily skew the various fit measures (i.e., the fit slope of 0.71 as compared to an ideal of 1 and mean difference, mean absolute difference, and root-mean-square difference of $4-6^{\circ}\text{C} \pm 3-4^{\circ}\text{C}$). If the most extreme values of MRT are not considered, all these fit measures improve substantially. In particular, for MRT between 35 and 65°C the fit slope increases to 0.94 while the mean difference, mean absolute difference, and root-mean-square difference reduce to 0.6±3.1°C, 2.3±2.2°C, and 3.2°C, respectively. Thus, the MRTs measured on an unobstructed roof site using the three-cylinder devices match closely with IRM values over the wide 35–65°C range but underpredict the values

by 5 to 15% for the extremely high MRT values of 65–80°C. Using geometrical weight factors for a sphere results in 2–5°C underprediction of lower values of the MRT and up to 6.5°C overprediction of the extreme values of the MRT.

287

288

289

290

291

292

293

294

295

296

297

298

299

300

301

302

303

304

305

306

307

308

309

284

285

286

Mid-day radiation measurements in diverse pedestrian-level urban sites in extreme heat conditions

We conducted mid-day measurements across thirteen pedestrian-level sites to complement the extended unobstructed roof site measurements. The fish-eye images in Fig.2E and characteristic descriptors in Table 1 and SI Section C.8 show that the sites included a wide diversity of microclimates. The shortwave, longwave, total radiative heat fluxes, and MRT measured using the IRM and two combinations of three cylinders are also reported in **Table 1**. In close agreement with prior measurements in nearby sites (Middel and Krayenhoff 2019), the MRT measured using the IRM ranges from slightly above that of air at 46.2°C (in the shade of a sizeable non-native tree) to 72.8°C (in a sun-exposed urban canyon with asphalt surface). The mean difference between the MRT from IRM and PHBW across the thirteen sites is $0.4\pm3^{\circ}$ C (±1 SD; mean absolute difference of 2.4±1.7°C and root mean square difference of 2.9°C), while that between the IRM and BHBW measurements is slightly higher at $1.7\pm4^{\circ}$ C (mean absolute difference of $3.4\pm2.5^{\circ}$ C and root mean square difference of 4.1°C). The difference between the MRT values obtained from the IRM and PHBW exceeds 4°C (at 6.7°C and for the BHBW method at 9.8°C) only at site 8, an urban canyon with a concrete surface and open sky. In this case, both combinations of the three cylinders overpredict the shortwave radiation by 60 to 70 W·m⁻² and underpredict the longwave radiation by 110 to 130 W·m⁻². However, these discrepancies did not occur in a similar but deeper urban canyon (site 13) with mostly asphalt rather than a concrete surface. It is important to highlight that even these discrepancies are within the substantial measurement uncertainty of the three-cylinder method. This measurement uncertainty mainly stems from our choice of the cylinder surface temperature sensor, highlighted in the Discussion section.

310

311

312

313

314

Discussion

Radiation measurements using the three-cylinder method: the good and the bad

Across a wide range of MRT and diverse micro-climates, the radiation measurements with the three-cylinder method closely match the IRM's. To put the $0.4\pm3.0^{\circ}$ C mean difference between

the MRT from IRM and PHBW cylinder combination into perspective, in our prior study comparing a variety of globe and cylinder radiometers to the IRM, we found mean differences of up to 6.5°C with standard deviation reaching 8°C (Vanos et al. 2021). Similarly, three-globe measurements closely matched those from the pyranometer-pyrgeometer setup (only upwards and downward facing) (Nakayoshi et al. 2015a). In terms of projected radiation area factors, it is evident that cylinders are a better representation of a human body than a sphere. In practice, when all directional fluxes are weighted, the primary difference is that globes are likely to overpredict radiation received by the human body when downward (incoming) and upward (outgoing or reflected) shortwave radiation is most intense. In other words, when the solar elevation angle is high, the globes can overpredict the MRT by up to 6.5°C compared to a cylinder. Besides this purely geometrical factor, Nakayoshi et al. (2015a) and others (Vanos et al. 2021) reported that substantial errors in globe radiometer measurements could be caused by placing the temperature sensor in the center of the air-filled devices (i.e., the measured internal temperature does not equal the average surface temperature). Such issues are resolved by placing the thermocouple on the surface of the thin yet sufficiently small isothermal cylinder. The cylindrical shape also enables the insertion and attachment of flexible rectangular heaters that internally provide uniform heat flux (vs. local attachment of a heater to a sphere).

For extreme values of the MRT (above about 70°C), the three-cylinder method can underpredict the MRT as compared to IRM by 5 to 10°C or about 5 to 15%. While this underprediction is within the experimental uncertainty of the three-cylinder measurements, the primary reason underlying this discrepancy is likely related to the mounting of the cylinders. Specifically, the cylinders are bottom mounted using a 2.5 cm diameter wooden dowel secured using another aluminum cylinder and a horizontal bracket (see **Fig.2 C**). Consequently, the bottoms of the cylinders have limited exposure to the intense long wave heat flux emitted by the roof's surface. Even with a small geometrical weight, this longwave radiation component contributes about $40 \text{ W} \cdot \text{m}^{-2}$ of the about $100 \text{ W} \cdot \text{m}^{-2}$ observed discrepancy between IRM and three-cylinder measurement (i.e., $0.06 \cdot 650 \approx 40 \text{ W} \cdot \text{m}^{-2}$). Since longwave heat flux is heavily absorption-weighted (i.e., $\alpha_{L-MRT} = 0.97$) in the MRT calculation, its underprediction by the three-cylinder methods propagates into underpredicted radiant temperature values. Other factors contributing to this discrepancy could include minor local differences in the MaRTy and three-cylinder array locations (i.e., slightly varying roof slope and distance to edges Despite being mounted from the

bottom, Nakayoshi et al. (2015a) globes were larger than the holding cylinder and captured a larger fraction of the outgoing radiation (i.e., did not underpredict the longwave radiation emitted by hot surfaces like the cylinders).

From convection coefficient to wind speed measurements: use of three cylinders as a low-speed anemometer

In contrast to our cylinder observation, Nakayoshi et al. (2015a) found that the heat transfer coefficients for their globes were impacted by turbulence intensity. Therefore, they developed an empirical fit for their data to predict wind speed as a function of the measured heat transfer coefficient. Since we observed that the heat transfer coefficient does not depend on turbulence intensity for the cylinder setup (see physical explanation in the SI), we can use the classical Hilpert correlation (Hilpert 1933). By substituting air properties and the cylinder diameter, we can simplify the Hilpert correlation to $h = 33\overline{V}(t)^{0.466}$. We note that the coefficient in this expression has a negligible variation with air temperature in the range of 20°C to 60°C. By flipping this expression, we can use the measured value of the heat transfer coefficient to calculate the time-varying mean air speeds as:

$$\overline{V}(t) = h^{2.146}/1814$$
 (4)

The uncertainty of this wind speed measurement is h^{1.146}U_h/845 for an U_h uncertainty in the heat transfer coefficient. The plot in **Fig.5** C shows good agreement between the detrended timevarying mean velocity measured using the 3D anemometer and that predicted using **Eq.4**. The agreement between the parameters improves (i.e., an increase in the fit slope from 0.85 to 0.93) when only data in low wind speed regime is considered (0.2 and 1.5 m·s⁻¹). Yet, when the measurement's uncertainty is considered, the proposed approach seems less appealing. For velocities above 1.5 m·s⁻¹, the uncertainty can be a substantial fraction of the predicted wind speed value (an average of 35%, as shown in the SI Section C.6 when all three cylinder measurements are considered). However, when the measurements are considered for each cylinder separately, a significant difference in the uncertainty range emerges (see the SI Section C.6). In particular, the uncertainty of the estimated wind speed using the PHBW combination is much smaller (an average of 20% of the measurement value). Employing only the data from the PHBW combination of cylinders to calculate the wind speed using **Eq.4** provides a substantial narrowing of the uncertainty band to a range of about 20% that is comparable to many lower-end commercial

anemometers (e.g., $1\pm0.2 \text{ m}\cdot\text{s}^{-1}$ or $1.5\pm0.3 \text{ m}\cdot\text{s}^{-1}$). We discuss the underlying reason and potential solutions for such a significant difference in the measurement uncertainty between these two approaches in the Limitations sections.

380

381

382

383

384

385

386

387

388

389

390

391

392

393

394

395

396

397

398

399

400

401

402

377

378

379

Limitations and potential improvements

Despite T-type thermocouples having the best accuracy $(\pm 1^{\circ}\text{C})$ of all the base metal thermocouples (ASTM E230/E230-17 2017), their use limits the achievable uncertainty of the three-cylinder measurements. The difference in the heat transfer coefficient uncertainty, and thereby the estimated wind speed, between the two combinations of cylinders illustrates the improvement that can be obtained by employing sensors with even tighter accuracy. In particular, the h_{PHRW} (Eq.I.12 in SI Section I.2) and associated uncertainty calculations (Eq. A10 in SI Section A) include the air temperature, which is measured using a PT-100 resistive thermal device (RTD) IEC 751 1/3 Class B with an accuracy of ± 0.1 °C (that is periodically validated with factory calibration). In contrast, the h_{BHBW} (Eq.I.6 in SI Section I.2) and associated uncertainty (Eq. A13 in SI Section A) calculations only incorporate the temperatures of the unheated and heated black cylinders, measured using the T-type thermocouples. Consequently, using RTDs instead of thermocouples to measure the surface temperature of the cylinders would substantially reduce the uncertainty of the heat transfer coefficient and radiative heat fluxes. Even further improvement might be obtained by a more significant redesign of the devices to include a custom RTD distributed over the entire cylinder surface. We note that this approach could also resolve many issues with the globe thermometers. Illustrating the feasibility of such devices, in our prior work on stretchable heat exchangers (Kotagama et al. 2020), we made a custom temperature sensor using a commercial steel extension spring embedded into a soft silicone tube. To address the underprediction of the longwave radiation emitted by hot surfaces that we observed on the roof site measurements, a redesign of the device could also include a side mounting of the cylinder. However, the impact of such modifications on the convective measurements would have to be quantified before field deployment.

403404

405

406

407

Conclusions

We demonstrated that shortwave and longwave radiation fluxes measured using the introduced three-cylinder devices closely match those of a state-of-the-art mobile biometeorological station

in most studied sites. Therefore, as the three-globe devices (Nakayoshi et al. 2015a, b), these simple three-cylinder devices can be used in many applications instead of expensive pyranometers and pyrgeometers (dependent on the data logger cost, the cylinder setup costs about one to two orders of magnitude less). From a purely geometrical perspective, the primary difference between radiation measured using spherical and cylindrical devices will occur when exposed to strong downward and upward fluxes (e.g., from 9:00 to 15:00 h, globes would overpredict MRT by 6.5°C). We also demonstrated that, as the three-globes, the combination of three cylinders can be used as a low-speed anemometer. Thus, this novel three-cylinder method is a promising, cost-effective, and easy-to-fabricate approach for local micro-climate characterization needed to include radiation and windspeed in assessing human thermal exposure to extreme heat.

417418

419

408

409

410

411

412

413

414

415

416

Acknowledgments

- 420 This research was supported by the National Science Foundation Leading Engineering for
- 421 America's Prosperity, Health, and Infrastructure (LEAP HI) #2152468 award. We thank Prof. Zach
- Holman and Mason Mahaffey for help measuring spectral distribution of LED panel used for
- calibration experiments. The authors gratefully acknowledge the use of spectroscopy equipment
- 424 within the Eyring Center for Solid State Science at Arizona State University. We would also like
- 425 to thank Mr. Duane Rider from ASU for advising how to properly and safely set up the roof site
- on the Walton Center for Planetary Health.

427

428

Author contributions

- 429 KR: conceptualization, experiments, analysis, manuscript writing and editing; AJ: field
- 430 experiments and analysis; KS: field experiments and optical property characterization; SHV, SSG,
- 431 MG, AKJ, KK, GP: wind tunnel experiments and analysis; RB: field experiments; JKV and AM:
- analysis, conceptualization and manuscript writing and editing.

433

434

435

References

- 436 ASTM E230/E230-17 (2017) Standard Specification for Temperature-Electromotive Force (emf)
- Tables for Standardized Thermocouples
- Bergman TL, Lavine AS, Incropera FP, Dewitt DP (2011) Fundamentals of heat and mass transfer.
- John Wiley & Sons, Inc, New York

- Brown RD (2019) Correcting the Error in Measuring Radiation Received by a Person: Introducing
 Cylindrical Radiometers. Sensors 19:5085
- Brown RD, Gillespie TJ (1986) Estimating outdoor thermal comfort using a cylindrical radiation thermometer and an energy budget model. Int J Biometeorol 30:43–52
- De Dear R (1988) Ping-pong globe thermometers for mean radiant temperatures. H and V Engineer 60:10–11
- 446 Fanger PO (1972) Thermal Comfort. McGraw-Hill Book Company, New York
- Fiala D, Havenith G (2015) Modelling human heat transfer and temperature regulation. In: The mechanobiology and mechanophysiology of military-related injuries. Springer, pp 265–302
 - Fiala D, Lomas KJ, Stohrer M (1999) A computer model of human thermoregulation for a wide range of environmental conditions: the passive system. J Appl Physiol
- Hilpert R (1933) Heat transfer from cylinders. Forsch Geb Ingenieurwes 4:215
- Höppe P (1992) Ein neues Verfahren zur Bestimmung der mittleren Strahlungstemperatur im Freien. Wetter und Leben 44:147–151
 - Kenny NA, Warland JS, Brown RD, Gillespie TJ (2008) Estimating the radiation absorbed by a human. Int J Biometeorol 52:491–503
 - Kotagama P, Manning KC, Rykaczewski K (2020) Fundamentals of soft thermofluidic system design. Soft Matter 16:6924–6932. https://doi.org/10.1039/D0SM00504E
 - Middel A, Krayenhoff ES (2019) Micrometeorological determinants of pedestrian thermal exposure during record-breaking heat in Tempe, Arizona: Introducing the MaRTy observational platform. Science of the total environment 687:137–151
- Nakayoshi M, Kanda M, de Dear R (2015a) Globe Anemo-radiometer. Boundary Layer Meteorol 155:209–227
 - Nakayoshi M, Kanda M, Shi R, de Dear R (2015b) Outdoor thermal physiology along human pathways: a study using a wearable measurement system. Int J Biometeorol 59:503–515
 - Nazarian N, Krayenhoff ES, Bechtel B, et al (2022) Integrated assessment of urban overheating impacts on human life. Earths Future 10:e2022EF002682
 - Ono T, Murakami S, Ooka R, Omori T (2008) Numerical and experimental study on convective heat transfer of the human body in the outdoor environment. Journal of Wind Engineering and Industrial Aerodynamics 96:1719–1732
 - Park S, Tuller SE (2011) Human body area factors for radiation exchange analysis: standing and walking postures. Int J Biometeorol 55:695–709
- 472 Parsons K (2019) Human heat stress. CRC Press

450

454

455

456

457

458

459

460

463

464

465

466

467

468

469

470

- Parsons K (2014) Human thermal environments: the effects of hot, moderate, and cold environments on human health, comfort, and performance. CRC press
- 475 Rykaczewski K, Bartels L, Martinez DM, Viswanathan SH (2022a) Human body radiation area factors for diverse adult population. Int J Biometeorol 66:2357–2367
- 477 Rykaczewski K, Vanos JK, Middel A (2022b) Anisotropic radiation source models for computational thermal manikin simulations based on common radiation field measurements. Build Environ 208:108636
- Staiger H, Matzarakis A (2020) Accuracy of mean radiant temperature derived from active and passive radiometry. Atmosphere (Basel) 11:805

482 483	Tabrizi AB, Whale J, Lyons T, Urmee T (2015) Rooftop wind monitoring campaigns for small wind turbine applications: Effect of sampling rate and averaging period. Renew Energy 77:320–
484	330
485	Thorsson S, Lindberg F, Eliasson I, Holmer B (2007) Different methods for estimating the mean
486	radiant temperature in an outdoor urban setting. Int J Climatol 27:1983–1993
487	Vanos JK, Rykaczewski K, Middel A, et al (2021) Improved methods for estimating mean radiant
488	temperature in hot and sunny outdoor settings. Int J Biometeorol 65:967–983
489	Viswanathan SH, Martinez DM, Bartels L, et al (2023) Impact of human body shape on forced
490	convection heat transfer. Int J Biometeorol 1–9
491	Wang S, Li Y (2015) Suitability of acrylic and copper globe thermometers for diurnal outdoor
492	settings. Build Environ 89:279–294. https://doi.org/10.1016/j.buildenv.2015.03.002
493	Xu J, Psikuta A, Li J, et al (2021) A numerical investigation of the influence of wind on convective
494	heat transfer from the human body in a ventilated room. Build Environ 188:107427
495	Yu Y, Liu J, Chauhan K, et al (2020) Experimental study on convective heat transfer coefficients
496	for the human body exposed to turbulent wind conditions. Build Environ 169:106533
497	Zhou S, Niu J (2022) Measurement of the convective heat transfer coefficient of the human
498	body in the lift-up design. In: E3S Web of Conferences. EDP Sciences, p 03001
499	Zhou S, Yu Y, Niu J (2022) Field Measurement of the Human Body Convective Heat Transfer
500	Outdoors. Available at SSRN 4283460
501	Zou J, Liu J, Niu J, et al (2020) Convective heat loss from computational thermal manikin subject
502	to outdoor wind environments. Build Environ 107469
503	Zou J, Yu Y, Liu J, et al (2021) Field measurement of the urban pedestrian level wind turbulence.
504 505	Build Environ 194:107713
506	
507	
508	
509	
510	
511	
512	
513	
514	
515	
516	
517	
518	
519	

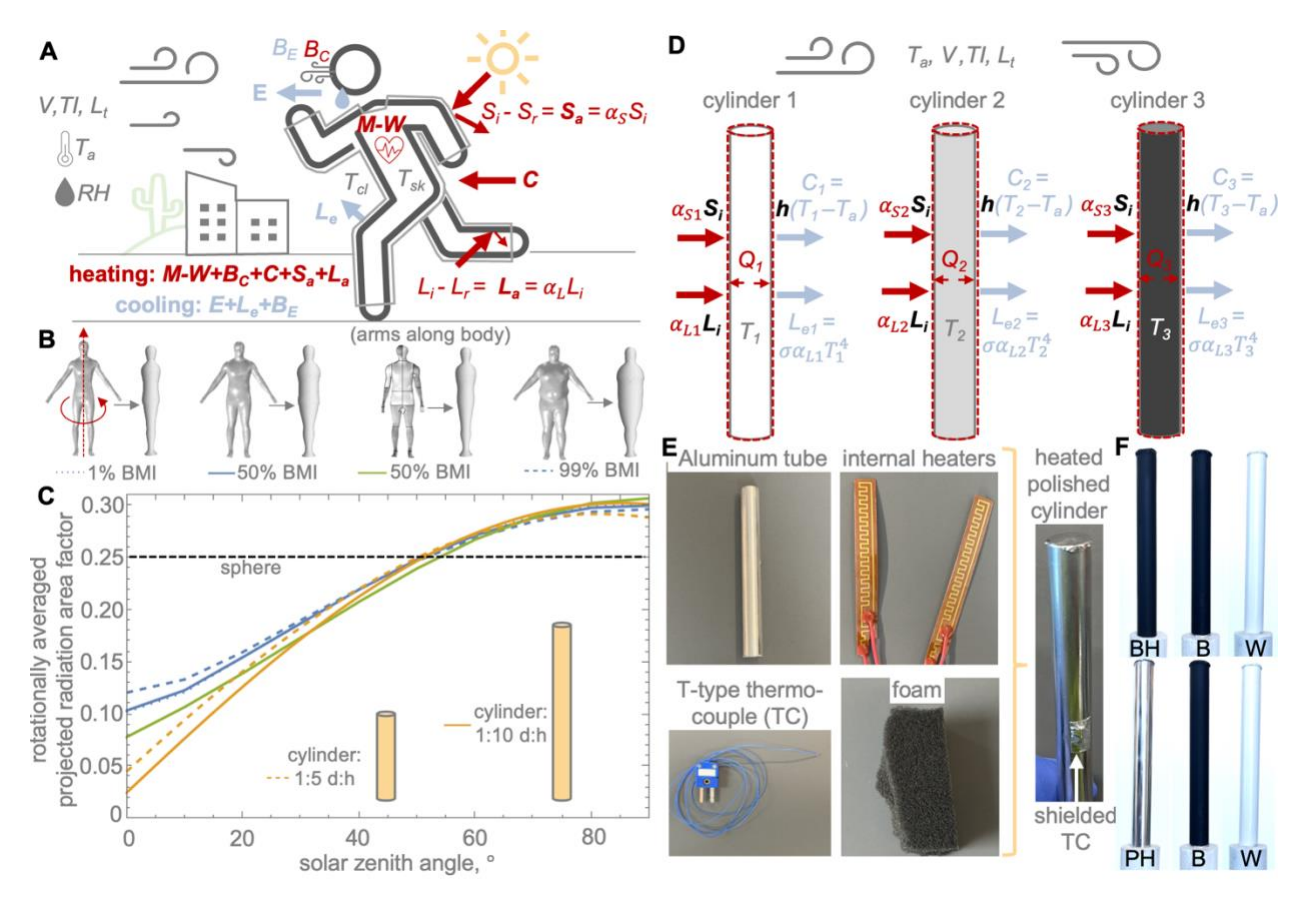


Fig.1 A. Primary environmental cooling and heating interactions with the human body in extremely hot conditions (when air temperature is greater than that of skin or about 35-37°C). Definitions: M-W-metabolic heat generation minus work output, C-convection, E-evaporation, B_C -sensible respiration, B_E -latent respiration contribution; radiation: S-shortwave, L-longwave, i-incident, r-reflected, a-absorbed, e-emitted, α_S -shortwave absorptivity, α_L -longwave absorptivity; V-air speed; TI-turbulence intensity; L_T -turbulence length scale; **B.** 3D rotationally averaged manikins of 1%, 50%, and 99% body mass index male with average height (Rykaczewski et al. 2022a), and **C.** plot of corresponding projected radiation area factors, a measure of the fraction of body surface area exposed to direct solar radiation, as a function of solar zenith angle; **D.** simultaneous air and surface temperature measurements with three cylinders yield three energy balances with three unknowns (h-heat transfer coefficient, S_i -incident short wave and L_i -incident longwave radiation) that can be solved for (Q-internal heater input), **E.** The main components before and after assembly into a heated polished cylinder (see the SI for step-by-step assembly), and **F.** images of the two combinations of three cylinders used in this study: black heated (BH), black (B), and white (W) as well as polished heated (PH), black (B) and white (W).

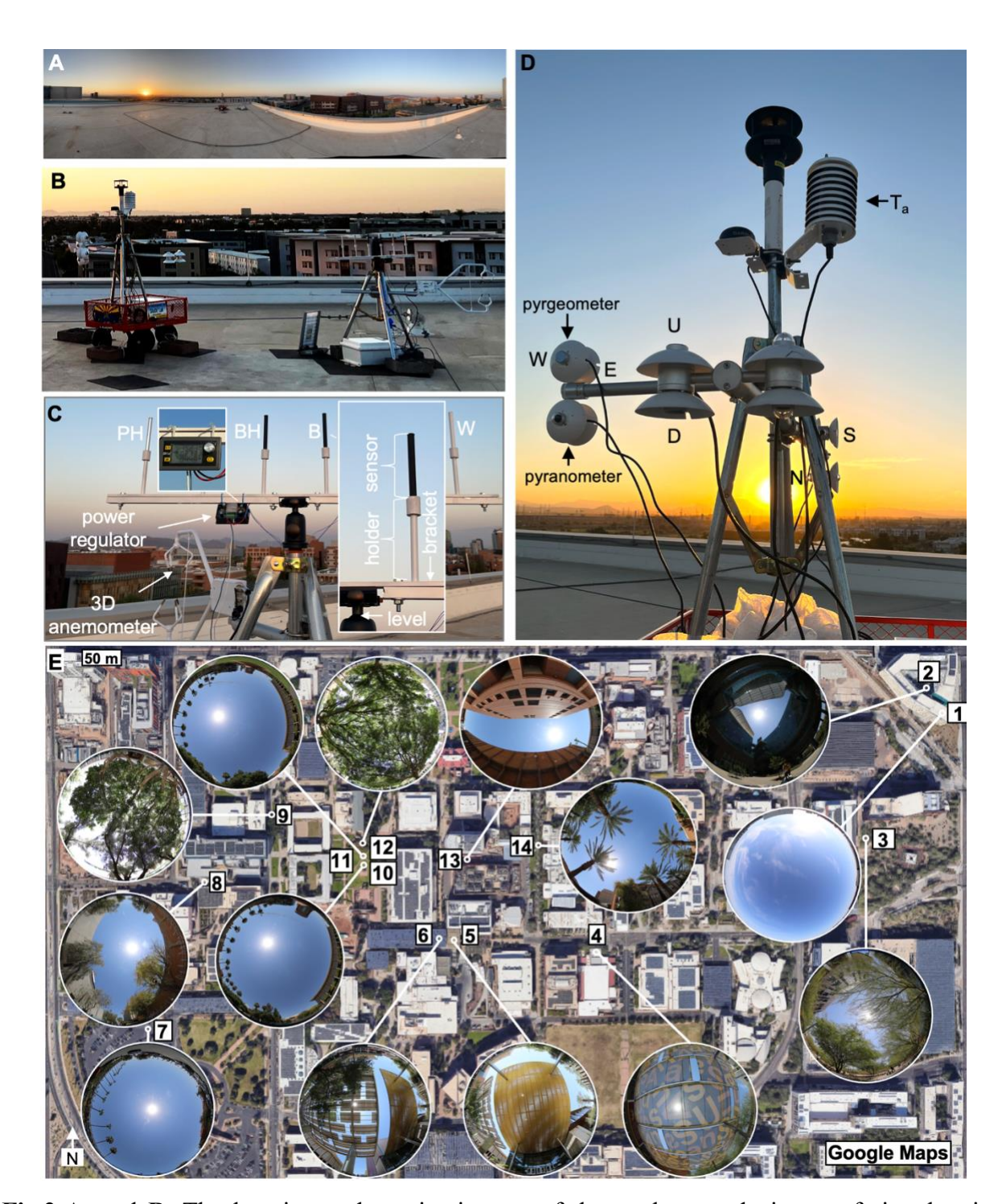


Fig.2 A. and **B.** The location and sunrise images of the unobstructed view roof site showing placement of MaRTy and tripod (1.5 m apart) with the cylinder array and 3D ultrasonic anemometer; **C.** close up of the cylinder tripod with marked details, and **D.** close up of MaRTy with marked details (pyranometer and pyrgeometers face cardinal directions: E-east, W-west, S-south, N-north; facing up-U, facing down-D); **E.** The location and bottom-up fish-eye images of all the measurement sites in Tempe, Arizona.

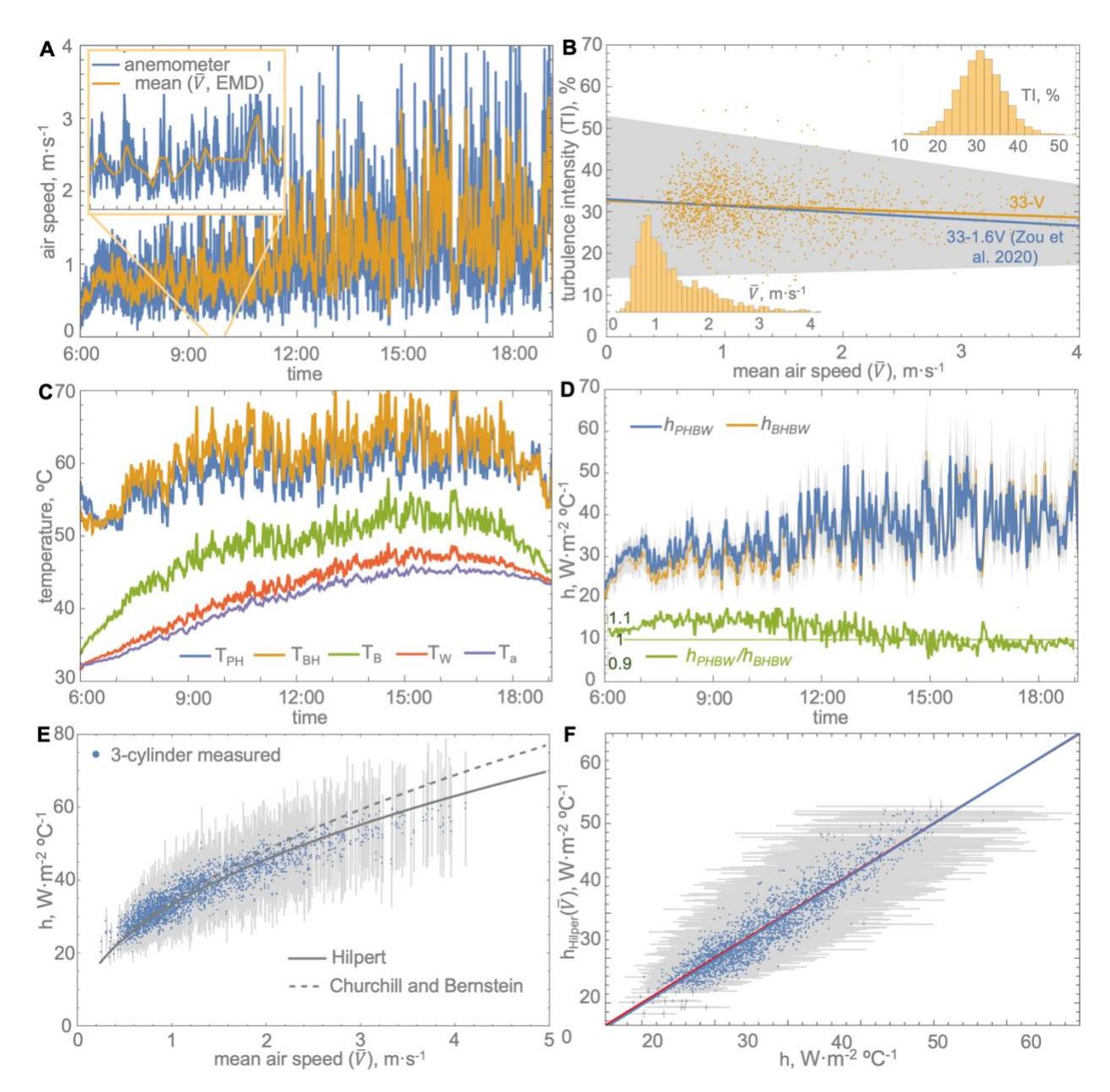


Fig.3 A. Timeseries of the raw 20 Hz wind speed measured using the anemometer (blue line) and Empirical Mode Decomposition (EMD) detrended time-varying mean velocity ($\bar{V}(t)$) (orange line) on July 25th; **B.** the detrended turbulence intensity (TI) variation with $\bar{V}(t)$ (insets show histograms of the TI and \bar{V} for all measurements; fit to our data ($TI = 33 - \bar{V}(t)$) as well as that from Zou et al. (2020) ($TI = 33 - 1.6\bar{V}(t)$) are also plotted; **C.** The air and surface cylinder temperatures (PH-polished heated, BH-black heated, B-black, W-white, a-air) and **D.** corresponding heat transfer coefficient calculated using BHBW and PHBW methods throughout July 25th (inset shows the ratio of the two); the variation of all heat transfer coefficient using the 3-cylinder methods with **E.** \bar{V} and **F.** heat transfer coefficient calculated using the Hilpert correlation employing \bar{V} .

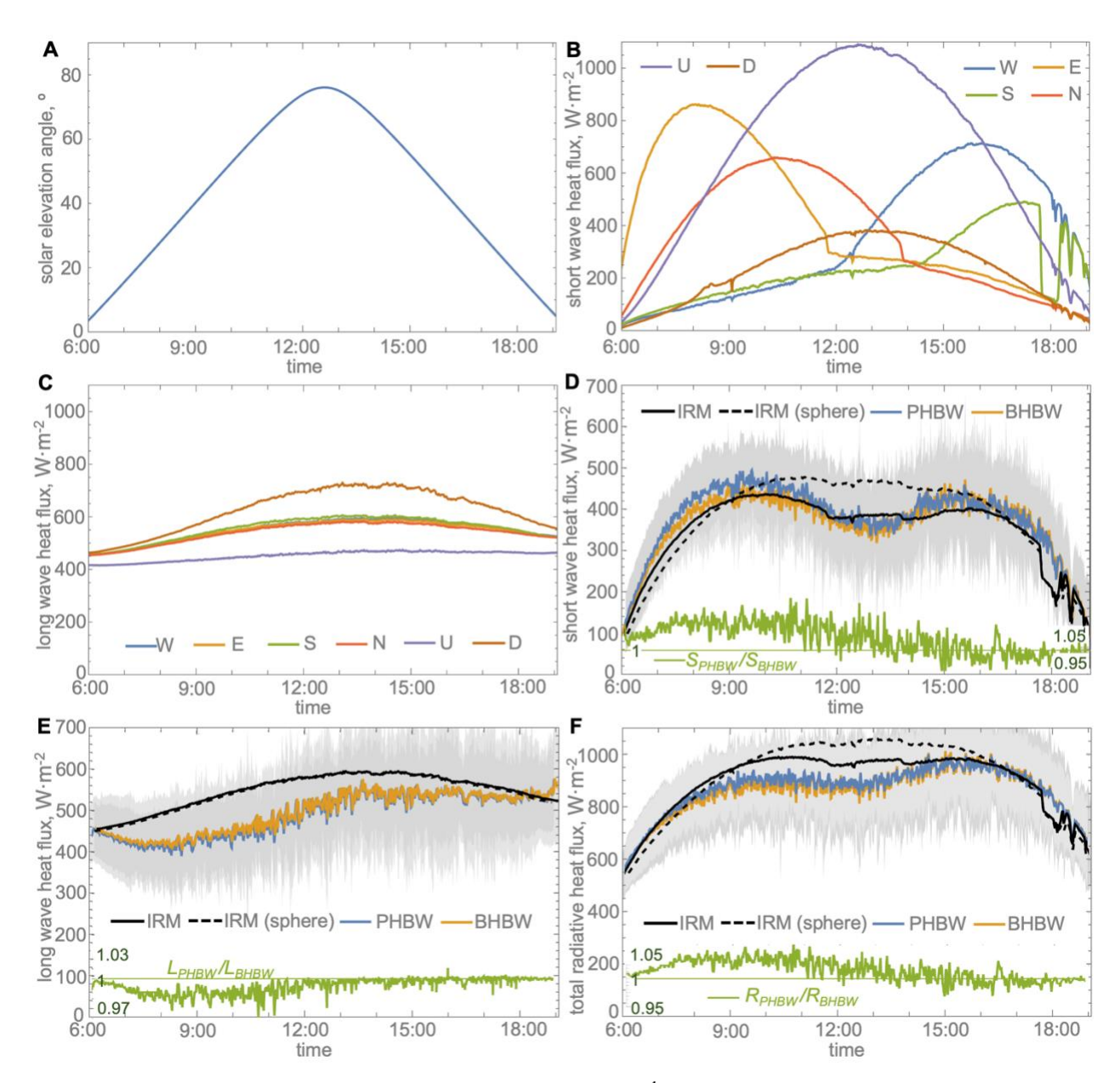


Fig.4 Time series of radiation observations on July 25th, 2023, of **A.** the solar elevation angle variation; the **B.** shortwave and **C.** longwave heat fluxes measured using MaRTy's detectors (facing cardinal directions: E-east, W-west, S-south, N-north; facing up-U, facing down-D); the individual directional fluxes are combined using IRM geometrical weights (**Eqs. 7-8**) (values for spherical shape weights are also shown) and compared against results of the PHBW and BHBW three-cylinder methods in **D.** shortwave spectral regime, **E.** longwave spectral regime, and **F.** in total terms (sum of short- and longwave fluxes). The insets in D-F panels show the ratio of the values stemming from PHBW and BHBW methods.

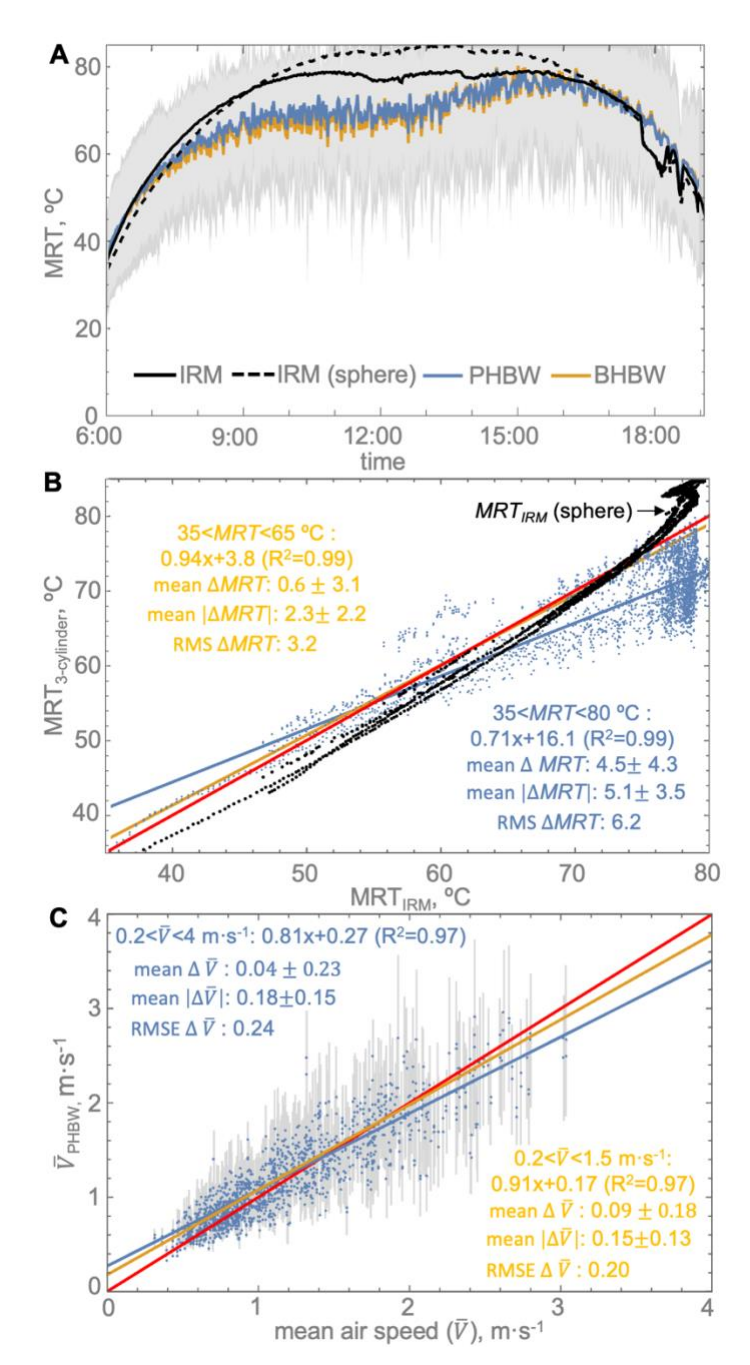


Fig.5 A. The time series of the mean radiant temperature (MRT) during July 25th of 2023, measured using IRM (MaRTy), PHBW, and BHBW three-cylinder combinations, and **B.** All MRTs obtained using the three-cylinder methods compared against ones measured using IRM; linear fit for full MRT range (blue line), and 35°C to 65°C range (orange line) are shown along with associated mean difference (Δ MRT \pm 1 standard deviation), mean absolute difference (Δ MRT| \pm 1 standard deviation), and root-mean-square (RMSE Δ MRT), and **C.** the air speed calculated using heat transfer coefficients with the PHBW combination of cylinders compared against the measured and detrended mean air speed for all collected measurements.

Table 1. The incident shortwave (S), longwave (L), and total (R_t=S+L) radiation fluxes (units: W·m⁻²) with corresponding mean radiant temperature (MRT, units: °C) measured on July 26th of 2023 between 12:00 and 14:30 h using MaRTy/IRM and the PHBW and BHBW three-cylinder combinations across the fourteen sites in Tempe, Arizona.

site	surface type	sky condition		MaRT	Гу/IRM		3-cylinder: PHBW				3-cylinder: BHBW			
1	white rubber	open sky (roof)	Rt	S	L	MRT	Rt	S	L	MRT	Rt	S	L	MRT
2	concrete	courtyard with open sky	844	266	577	68.1	856	226	630	70.7	871	265	606	71.2
3	concrete	Parkinsonia aculeata (native tree)	746	160	586	60.4	768	265	503	59.5	721	231	491	55.0
4	concrete	sun sail	689	111	578	55.1	716	214	503	54.9	703	221	482	53.0
5	brick	perforated metal shade	632	40	592	50.3	676	85	591	54.4	674	112	562	53.2
6	concrete	solar panel shade	639	44	595	51.1	668	90	577	53.1	662	113	549	51.6
7	asphalt	open sky	855	235	620	70.4	896	318	578	72.3	891	341	550	71.1
8	concrete	urban canyon with open sky	876	263	614	71.9	834	329	505	65.1	805	319	486	62.1
9	concrete	Ficus macrocarpa (non-native tree)	597	26	570	46.2	619	87	532	46.9	616	108	508	45.6
10	grass	open sky	838	303	535	66.4	838	363	474	64.4	824	372	451	62.5
11	concrete sidewalk on grass	open sky	868	296	572	69.9	851	344	507	66.6	842	361	481	65.0
12	grass	Juglans major (native tree)	622	62	560	48.2	624	106	518	46.8	619	124	495	45.5
13	asphalt	urban canyon with open sky	879	240	639	72.8	841	224	618	69.2	849	259	591	69.0
14	concrete	Phoenix canariensis (non-native tree)	754	168	586	61.0	766	170	597	62.4	810	242	568	65.1